ELSEVIER

Chemical Engineering Science 59 (2004) 2535–2545

Chemical Engineering Science

www.elsevier.com/locate/ces

CFD simulations of mass transfer from Taylor bubbles rising in circular capillaries

J.M. van Baten, R. Krishna*

Department of Chemical Engineering, University of Amsterdam, Nieuwe Achtergracht 166, 1018 WV Amsterdam, The Netherlands

Received 16 December 2003; received in revised form 16 March 2004; accepted 16 March 2004

Abstract

Computational Fluid Dynamics (CFD) is used to investigate mass transfer from Taylor bubbles to the liquid phase in circular capillaries. The liquid phase volumetric mass transfer coefficient k_La was determined from CFD simulations of Taylor bubbles in upflow, using periodic boundary conditions. The separate influences of the bubble rise velocity, unit cell length, film thickness, film length, and liquid diffusivity on k_La were investigated for capillaries of 1.5, 2 and 3 mm diameter. The mass transfer from the Taylor bubble is the sum of the contributions of the two bubble *caps*, and the *film* surrounding the bubble. The Higbie penetration model is used to describe the mass transfer from the two hemispherical caps. The unsteady-state diffusion model of Pigford is used to describe the mass transfer to the downward flowing liquid film. The developed model for k_La is in good agreement with the CFD simulated values, and provides a practical method for estimating mass transfer coefficients in monolith reactors.

Keywords: Taylor bubbles; Mass transfer; Capillary; Penetration model; Thin films; CFD; Monolith reactors

1. Introduction

Monolith loop reactors are gaining considerable attention from academia and industry alike for carrying out solid catalyzed gas–liquid reactions (Boger et al., 2003; Crynes et al., 1995; Irandoust and Andersson, 1988a; Kapteijn et al., 2001). Monolith loop reactors are being applied in laboratory studies and in commercial practice for carrying out reactions such as hydrogenations (Edvinsson and Cybulski, 1995; Edvinsson et al., 1995; Nijhuis et al., 2003), hydrodesulphurization (Irandoust and Gahne, 1990), oxidations (Klinghoffer et al., 1998) and Fischer-Tropsch synthesis (de Deugd et al., 2003a,b). Monolith reactors offer many potential advantages over trickle beds, slurry bubble columns and airlifts that include low pressure drop, high mass transfer rates, and ease of scale up (Edvinsson and Cybulski, 1995; Kreutzer, 2003; Nijhuis et al., 2001; Stankiewicz, 2001). Provided the gas and liquid phases are uniformly distributed over the various channels of the monolith, commercial reactor of large dimensions can, in principle, be scaled up from information on the hydrodynamics, mass transfer, and mixing within a single channel that has dimensions typically in the 1–3 mm range. Inside each capillary, we usually have Taylor flow of gas bubbles, as shown schematically in Fig. 1a. In the development and design of monolith loop reactors for fast reactions, the mass transfer from the Taylor gas bubbles to the surrounding liquid phase becomes an important limiting factor (Heiszwolf et al., 2001; Irandoust and Andersson, 1988b, 1989; Irandoust et al., 1992; Kreutzer, 2003; Kreutzer et al., 2001). Reliable estimation of the liquid phase volumetric mass transfer coefficient k_La, for gas–liquid transfer, is essential in these cases.

Bercic and Pintar (1997) have put forward the following empirical correlation for estimation of k_La:

$$k_La = 0.111\,\frac{(U_G + U_L)^{1.19}}{((1-\varepsilon_G)L_{UC})^{0.57}}, \tag{1}$$

where U_G and U_L are the superficial velocities of the gas and liquid phases, ε_G is the gas holdup, and L_{UC} is the unit cell length. It is remarkable to note that the Bercic–Pintar correlation for k_La shows no dependence on the channel diameter, d_c. The liquid phase diffusivity, $Đ$, was not varied

---

* Corresponding author. Tel.: +31-20-525-7007; fax: +31-20-525-5604.

E-mail address: krishna@science.uva.nl (R. Krishna).

0009-2509/$ - see front matter © 2004 Elsevier Ltd. All rights reserved.
doi:10.1016/j.ces.2004.03.010

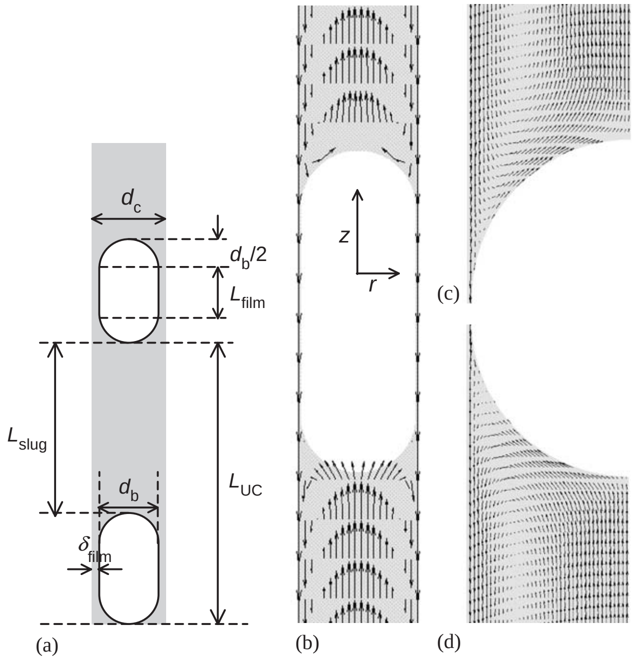

Fig. 1. (a) Schematic of Taylor bubble rise in a capillary. (b)–(d): Liquid velocity vectors obtained from CFD simulations for $d_c = 3$ mm, $V_b = 0.45$ m/s, $L_{UC} = 0.04$ m, $\delta_{\mathrm{film}} = 48$ μm, $\varepsilon_G = 0.17$, $L_{\mathrm{film}} = 5.31$ mm, $Đ = 1 \times 10^{-9}$ m^2/s.

in their experiments and, consequently, does not appear in Eq. (1). Irandoust et al. (Irandoust and Andersson, 1988b; Irandoust et al., 1992) and Kreutzer (2003) have adopted a more fundamental approach to the estimation of $k_L a$. They consider the separate contributions of the mass transfer from the two hemispherical caps, and transfer to the liquid flowing down the sides of the bubble. The channel diameter d_c does influence the $k_L a$ of both cap and film contributions in the Irandoust and Kreutzer approaches.

The major objective of the present work is to use Computational Fluid Dynamics (CFD) in order to study the *separate* influences on $k_L a$ of various hydrodynamic and system parameters such as bubble rise velocity V_b, L_{UC}, ε_G, $Đ$, and d_c. Such a study will provide insights into the mass transfer mechanisms and allow more reliable scale up of monolith reactors.

We begin with the development a *fundamental*, yet simple, model for estimation of $k_L a$. Subsequently, CFD simulations are used to validate this model. The CFD simulated $k_L a$ values are compared with the predictions of Eq. (1).

2. Model for mass transfer coefficient

We consider an idealized geometry for the Taylor bubbles, consisting of two hemispherical caps and a cylindrical body; see Fig. 1a. Experimental observations using a high-speed video camera with the air–water system confirm the idealized shape for Taylor bubbles (Vandu et al., 2004). The liquid phase velocity vectors (obtained from CFD simulations, to be discussed later, and in a reference frame with the bubble held stationary), are shown in Figs. 1b–d. Let us first consider mass transfer from either hemispherical cap to the surrounding liquid. The Higbie penetration model (see p. 153 of Sherwood et al. (1975)) provides a physical picture of the mass transfer process. For the top cap (Fig. 1c) a packet of liquid arriving at the wall will traverse upwards along the surface of the cap right to the nose before being engulfed into the bulk liquid "slug". Similarly, for the bottom cap (Fig. 1d), a liquid element arriving at the nose from the bulk liquid slug will be swept upwards along the cap surface right up to the liquid film at the wall. At this juncture the element will be swept downwards and away from the surface by the downflowing liquid. The average distance travelled by the liquid packet will be one-half of the bubble circumference, i.e. $(\pi d_b/2) \approx (\pi d_c/2)$ and the average contact time with the bubble, rising with a velocity V_b is $(\pi d_c/2V_b)$. The penetration model for mass transfer yields

$$k_{L,\mathrm{cap}} = 2\sqrt{2\,\frac{ĐV_b}{\pi^2 d_c}} = 2\,\frac{\sqrt{2}}{\pi}\,\sqrt{\frac{ĐV_b}{d_c}}. \tag{2}$$

A similar approach has been used by Kreutzer (2003) and Irandoust et al. (Irandoust and Andersson, 1988b; Irandoust et al., 1992), albeit with different coefficients preceding the square root sign. The volumetric mass transfer coefficient $k_{L,\mathrm{cap}} a_{\mathrm{cap}}$ is obtained by multiplying Eq. (2) with the specific interfacial area for the two hemispherical caps

$$a_{\mathrm{cap}} = \frac{4}{L_{UC}}. \tag{3}$$

We note that the bubble diameter is related to the channel diameter by

$$d_b = d_c - 2\delta_{\mathrm{film}}, \tag{4}$$

where δ_{film} is the thickness of the film surrounding the bubble. The film thickness δ_{film} can be estimated from the following semi-empirical relation developed by Aussillous and Quere (2000)

$$\frac{\delta_{\mathrm{film}}}{d_c} = \frac{0.66\,Ca^{2/3}}{1 + 3.33\,Ca^{2/3}}; \qquad Ca \equiv \frac{\mu_L V_b}{\sigma}, \tag{5}$$

where Ca is the Capillary number. For the air–water system and the range of bubble rise velocities and capillary diameters in the 1–3 mm range, as encountered in practice, the film thickness δ_{film} is of the order of 30–90 μm.

The second contribution to mass transfer is due to the film surrounding the bubble of length, L_{film}. Depending on the value L_{film} and the contact time the transferring component can penetrate deep into the film. Pigford, in his 1941 Ph.D.

thesis analyzed the transient mass transfer to a falling film in laminar flow; his analysis is most conveniently found on p. 206 of Sherwood et al. (1975). The mass transfer coefficient is given by

$$k_{L,\text{film}} = \frac{Q_{\text{film}}}{\pi d_c L_{\text{film}}} \ln\left(\frac{1}{\Delta}\right), \tag{6}$$

where Q_{film}, is the volumetric flow of the liquid film down the walls and

$$\begin{aligned}\Delta &= 0.7857\exp(-5.121Fo) + 0.1001\exp(-39.21Fo)\\ &\quad + 0.0360\exp(-105.6Fo) + 0.0181\exp(-204.7Fo)\\ &\quad + \ldots,\end{aligned} \tag{7}$$

where the Fourier number is defined as

$$Fo \equiv \frac{Đ}{t_{\text{film}}\delta_{\text{film}}^2} \tag{8}$$

and t_{film} is the contact time of the liquid film with the rising Taylor gas bubble. This contact time can be evaluated if the velocity of the falling liquid film is known or can be estimated (Thulasidas et al., 1995). In practice, it is more convenient to evaluate $k_{L,\text{film}}$ for the limiting cases of Eq. (6) for (a) $Fo < 0.1$, and (b) $Fo > 0.1$ corresponding to short and long contact times respectively.

$$\begin{aligned}k_{L,\text{film}} &= 2\sqrt{\frac{Đ}{\pi t_{\text{film}}}\frac{\ln(1/\Delta)}{(1-\Delta)}}; \quad Fo < 0.1 \quad \text{(short contact)}\\ k_{L,\text{film}} &= 3.41\frac{Đ}{\delta_{\text{film}}}; \quad Fo > 1 \quad \text{(long contact)}.\end{aligned} \tag{9}$$

For long film contact times with $Fo > 0.8$ and $\Delta \to 0$, the liquid film approaches saturation and its contribution to the overall mass transfer process will be increasingly ineffective. For all the CFD simulations to be reported later in this paper, the conditions corresponded to $Fo < 0.1$, i.e. short contact time and in no case was the film saturated. The models of Kreutzer (2003) and Irandoust et al. (Irandoust and Andersson, 1988b; Irandoust et al., 1992) for $k_{L,\text{film}}$ are based on the film model and therefore applicable only for long contact times.

The volumetric mass transfer coefficient for the film $k_{L,\text{film}}a_{\text{film}}$ is obtained by multiplying either of the limiting solutions in Eq. (9) with the specific interfacial area of the film

$$a_{\text{film}} = 4\frac{L_{\text{film}}}{d_c}\frac{1}{L_{UC}}. \tag{10}$$

It is clear from Eqs. (2), (3), (9) and (10) that the sum of the cap and film contributions to mass transfer will depend on several parameters: V_b, L_{UC}, L_{film}, t_{film}, δ_{film}, $Đ$, and d_c. It remains to resort to CFD simulations to verify the various dependencies forecast by the model developed above.

3. CFD model development

The Taylor bubble is considered as a "void", acting as a free surface with the surrounding liquid phase; see the computational domain pictured in Fig. 2a. The volume-averaged mass and momentum conservation equations in the Eulerian framework are given by

$$\nabla \bullet \mathbf{u}_L = 0, \tag{11}$$

$$\begin{aligned}\rho_L\frac{\partial \mathbf{u}_L}{\partial t} &+ \nabla \bullet (\rho_L \mathbf{u}_L \mathbf{u}_L - \mu_L(\nabla \mathbf{u}_L + (\nabla \mathbf{u}_L)^{\mathrm{T}}))\\ &= -\nabla p + \rho_L \mathbf{g},\end{aligned} \tag{12}$$

where ρ_L, $\mathbf{u}_L$ and μ_L. represent, respectively, the macroscopic density, velocity and viscosity of the liquid phase, p is the pressure and $\mathbf{g}$ is the gravitational acceleration. Laminar flow conditions are assumed to prevail.

A commercial CFD package CFX, version 4.4, of ANSYS, Inc., Canonsburg, USA was used to solve the equations of continuity and momentum. This package is a finite volume solver, using body-fitted grids. The grids are non-staggered and all variables are evaluated at the cell centres. An improved version of the Rhie–Chow algorithm (Rhie and Chow, 1983) is used to calculate the velocity at the cell faces. The pressure–velocity coupling is obtained using the SIMPLEC algorithm (van Doormal and Raithby, 1984). For the convective terms in Eqs. (11) and (12), the SUPERBEE- MUSCL differencing scheme was used (higher order upwind scheme with flux delimiters). A fully implicit

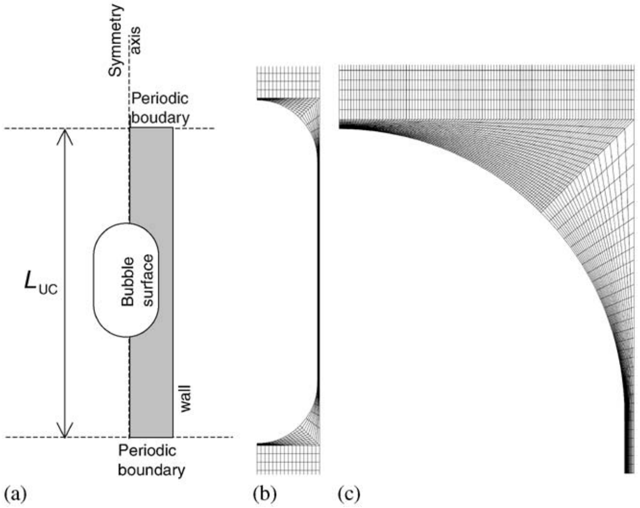

Fig. 2. (a) Schematic overview of the computational domain of unit cell with periodic boundary conditions at inlet and outlet. (b) Grid details for $d_c = 3$ mm, $V_b = 0.45$ m/s, $L_{UC} = 0.04$ m, $\delta_{\text{film}} = 48$ µm, $\varepsilon_G = 0.17$, $L_{\text{film}} = 5.321$ mm. (c) Close-up view of grid near the bubble edges. The cell size in the film decreases exponentially in the direction of the film to facilitate accurate capturing of the second order concentration gradient near the film. The grid details are specified in Table 1.

backward differencing scheme was used for the time integration.

The boundary condition was periodic in the vertical direction ($\mathbf{u}_{\text{top}} = \mathbf{u}_{\text{bottom}}, p_{\text{top}} = p_{\text{bottom}}$). The hydrostatic pressure drop of $\mathbf{g}\rho_L$ is added as a source term to the momentum balance equation (12) to correct for the periodic boundary conditions.

Simulations were performed in a reference frame in which the bubble is stationary and the system moves up with the bubble rise velocity V_b. At the outer wall, the boundary condition was set to $u_z = V_{\text{wall}} = -V_b$, $u_r = 0$, where r and z are the radial and axial coordinates. The bubble surface is specified as free-slip: $\mathrm{d}u_\perp/\mathrm{d}n = 0$, with $u_\perp$ being the velocity component in the direction of the bubble surface, and n is the normal direction to the bubble surface. At the axis of symmetry, we have $\mathrm{d}u_z/\mathrm{d}r = 0$.

The simulations were carried out using axi-symmetric 2D grids using cylindrical coordinates. The calculation of the volumetric mass transfer coefficient using CFD simulations was carried out in two consecutive campaigns for hydrodynamics (flow fields) and mass transfer, respectively. In the first campaign, the mass and momentum transfer equations were solved using periodic boundary conditions at the inlet and outlet to obtain the *steady-state* hydrodynamics. The steady state solutions were typically obtained within 10,000 iterations and it was verified that convergence was indeed obtained.

The average liquid velocity is calculated from a summation over the cells at the top boundary of the computational domain

$$u_{L,\text{domain}} = \frac{\sum_{\text{top}} \text{vol}_i u_i}{\sum_{\text{top}} \text{vol}_i}. \tag{13}$$

Here, vol_i is the volume of cell i and u_i is the vertical velocity in cell i. The summation in Eq. (13) is over the total number of cells at the top boundary. The *superficial* liquid velocity is now calculated from

$$U_L = (u_{L,\text{domain}} - V_{\text{wall}})(1 - \varepsilon_G), \tag{14}$$

where the gas holdup ε_G is the bubble volume divided by the unit cell volume.

$$\varepsilon_G = \frac{\text{bubble volume}}{L_{UC}\pi d_c^2/4}. \tag{15}$$

The superficial gas velocity is calculated from

$$U_G = \varepsilon_G V_b. \tag{16}$$

The volumetric flow of liquid through the thin film surrounding the bubble, Q_{film}, is calculated from the following relation derived by Thulasidas et al. (1995) using a mass balance over a cross section through the bubble and a cross section through the liquid slug

$$A_b V_b = A_c U_{LS} + Q_{\text{film}}, \tag{17}$$

where U_{LS} is the velocity of the liquid slug that is determined from

$$U_{LS} = u_{L,\text{domain}} - V_{\text{wall}}. \tag{18}$$

Rearranging Eq. (17) we get

$$Q_{\text{film}} = \frac{\pi}{4}(d_b^2 V_b - d_c^2 U_{LS}). \tag{19}$$

The film flow Q_{film} calculated from Eq. (19) agrees with the value obtained by integration of the velocity profile in the film between the bubble surface and the capillary wall.

The converged velocity field obtained was used in a subsequent mass transfer simulation campaign, carried out in a transient manner, for which 3000 time steps of 0.01 s were used. The tracer concentration throughout the system was initially set to zero. At $t = 0$, the tracer concentration at the bubble surface was set to unity (a.u.) to determine the mass transfer from the gas phase to the liquid phase. The following equation is solved for the mass tracer:

$$\frac{\partial}{\partial t}(\rho_L C_L) + \nabla \cdot (\rho_L \mathbf{u}_L C_L - Đ\rho_L \nabla C_L) = 0. \tag{20}$$

Here, C_L is the concentration of mass-tracer in the liquid (a.u.) and $Đ$ is the diffusion coefficient of mass tracer in the liquid. At the top and bottom, the periodic boundary conditions were used: $C_{L,\text{top}} = C_{L,\text{bottom}}$. Zero tracer flux was allowed through the outer wall: $\mathrm{d}C_L/\mathrm{d}r = 0$. Symmetry conditions apply to the center axis: $\mathrm{d}C_L/\mathrm{d}r = 0$. At the bubble surface, the concentration is specified as $C_{L,s} = 1$.

The total concentration of tracer in the system at each time step was determined from

$$C_{L,\text{system}} = \frac{\sum_{\text{domain}} \text{vol}_i C_{L,i}}{\sum_{\text{domain}} \text{vol}_i}, \tag{21}$$

where the summation is carried out over all the volume elements in the computational domain. The difference in the $C_{L,\text{system}}$ values at two consecutive time steps is used to determine the mass flux of tracer from the bubble to the domain (liquid). The volumetric mass transfer coefficient $k_L a$ is then calculated from

$$k_L a = \frac{\mathit{flux}}{(C_{L,s} - C_{L,\text{cupmix}})} \frac{(\text{bubble surface area})}{(\text{unit cell volume})}, \tag{22}$$

where the driving force for mass transfer is taken as the difference in the concentration at the bubble surface ($C_{L,s} = 1$) and the cup-mixed concentration of the liquid leaving the top boundary at that time

$$C_{L,\text{cupmix}} = \frac{\sum_{\text{top}} \text{vol}_i u_i C_{L,i}}{\sum_{\text{top}} \text{vol}_i u_i}. \tag{23}$$

The velocities u_i in Eq. (23) are the ones obtained from the simulations in the reference frame with the bubble held stationary and the wall moving at a velocity V_b. The u_i are the velocity fields the bubble experiences.

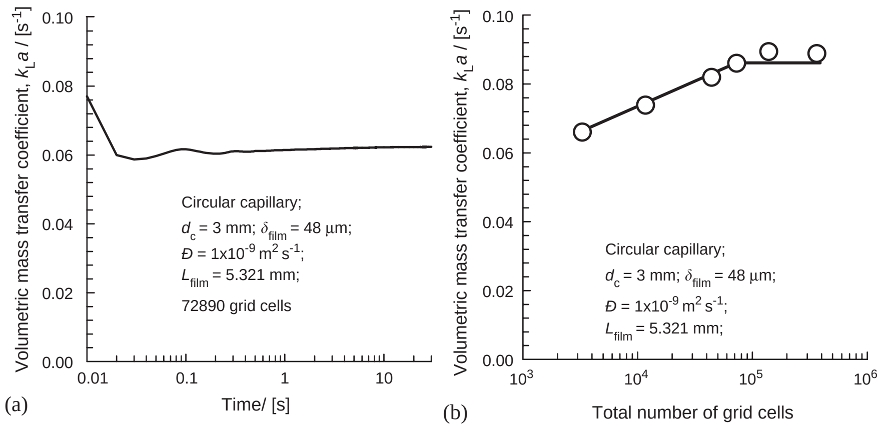

Fig. 3. (a) Values of $k_L a$ from transient mass transfer simulation campaign for $d_c = 3$ mm, $V_b = 0.45$ m/s, $L_{UC} = 0.04$ m, $\delta_{film} = 48$ μm, $\varepsilon_G = 0.17$, $L_{film} = 5.321$ mm. Animations showing the dynamics of mass transfer can be viewed on our website (van Baten and Krishna, 2004). (c) Variation of $k_L a$ with number of grid cells used for the computational domain.

Table 1
Details of variations of parameters and grid cells used in the simulations

d_c/ (mm)	L_{UC}/ (mm)	V_b/ (m/s)	L_{film}/ (mm)	δ_{film}/ (μm)	ε_G/ (−)	Total grid cells	Smallest cell size/(μm)
3	40	0.15, 0.2, 0.3, 0.45, 0.55	5.23	48	0.17	72890	1.00
3	50	0.15, 0.30, 0.45, 0.55	5.23	48	0.136	93090	1.00
3	35	0.30, 0.45, 0.55	5.23	48	0.194	62790	1.00
3	35, 40, 50	0.30	5.23	48	0.5	62790 – 93090	1.00
3	15, 20, 25, 30, 35, 40, 50	0.45	5.23	48	0.136 – 0.453	22390 – 93090	1.00
3	35, 40, 50	0.55	5.23	48	0.136 – 0.194	62790 – 93090	1.00
3	40	0.45	5.23, 5.74, 6.51, 10.77, 15.04, 19.31	48	0.17 – 0.5	51176 – 72890	1.00
3	40	0.45	5.23,5.74	10,48,100	0.17	70257 – 77300	0.5
2	40	0.15, 0.3, 0.45	5.90	32	0.170	50658	0.60
2	15, 25, 40	0.45	5.90	32	0.170 – 0.453	17158 – 50658	0.60
1.5	40	0.15, 0.3, 0.45	6.24	24	0.170	74912	0.40
1.5	15, 25, 40	0.45	6.24	24	0.17 – 0.453	24412 – 74912	0.40

For a typical run, with $d_c = 3$ mm, $V_b = 0.45$ m/s, $L_{UC} = 0.04$ m, $\delta_{film} = 48$ μm, $\varepsilon_G = 0.17$, $L_{film} = 5.321$ mm, the values of $k_L a$ calculated at each time step using Eq. (22) are shown in Fig. 3a. We note that the $k_L a$ reaches a quasi-steady state value after about 1 s and this is the value reported in this paper. We also tested grid convergence on the simulated $k_L a$ values; see Fig. 3b. Each simulation was carried out in three stages: (1) Solution of the steady-state hydrodynamics to obtain the velocity fields using a coarse grid with 3300 cells, (2) Using this converged velocity field as a *starting guess*, solution of the hydrodynamics for a *finer* grid, and (3) Transient mass transfer simulations using the converged velocity fields obtained with the *finer* grid. While a total of 3300 cells is adequate to obtain convergence on the velocity field in the first stage of the computations, we need at least 72890 cells to obtain $k_L a$ values that are within 5% of the final converged values. To correctly capture the steep concentration gradients near the bubble surface and in the film between the bubble and wall, we used a cell size smaller than 1 μm close the surface, with an exponential increase away from the surface as shown in Figs. 2b and c.

A total of 40 simulations with varying parameter values d_c, V_b, L_{UC}, L_{film}, δ_{film}, and $Đ$ were carried out on Linux PCs with a single AMD XP processor. The details of parameter values used in these simulations are listed in Table 1, along with the total number of grid cells and smallest cell size. Each hydrodynamic simulation on the coarse grid was solved in a matter of minutes, each hydrodynamic simulation on the fine grid took several hours. Each dynamic mass tracer run also took several hours. Animations showing the dynamics of mass transfer can be viewed on our website (van Baten and Krishna, 2004).

4. Discussion of simulation results for k_La

Consider first a simulation campaign in the 3 mm capillary with a unit cell length $L_{UC} = 0.04$ m, with varying values of the Taylor bubble rise velocity, V_b. The liquid phase velocity profiles at the top of the computational domain (liquid outlet) are shown in Fig. 4a, in the reference velocity frame with a stationary wall (these values are obtained by adding the bubble rise velocity to the values obtained from the simulations, e.g. shown in Figs. 1b–d). The velocity profiles are parabolic in shape with a maximum velocity at the centre of the channel that is twice the value of the liquid slug velocity, U_{LS}. The liquid velocity profiles within the film are shown in Fig. 4b. The velocity of the liquid at the surface of the film is one and a half times the average liquid velocity, in keeping with the classical solution for the velocity fields in falling films; see p. 78 of Sherwood et al. (1975). In Fig. 4c, we see that the magnitude of the velocity of the liquid film at the surface next to the Taylor bubble, V_{film}, increases linearly with V_b. Since the bubble rises upwards *counter-current* to the liquid film the contact time, t_{film}, between the bubble and the liquid film for a film of length L_{film} is to be calculated using $t_{\mathrm{film}} = L_{\mathrm{film}}/(V_b + V_{\mathrm{film}})$ where we note that V_{film} has a negative value, as shown in Fig. 4c. The value of $(U_G + U_L)$ is slightly smaller than the value of the bubble rise velocity, V_b and this is due to the backflow of liquid through the film as described by Eq. (17); see Fig. 4d. With increasing V_b the flow of liquid through the film surrounding the bubble, Q_{film} also increases, thus increasing backflow. This explains the increasing deviation between $(U_G + U_L)$ and V_b with increasing V_b.

With increasing values of V_b both $k_{L,\mathrm{cap}}$ and $k_{L,\mathrm{film}}$ are increased due to *shorter* contact time for *both* cap and film contributions, as can be seen by examination of Eqs. (2) and (6). As seen in Fig. 5a, the k_La values show a linear dependence on $\sqrt{V_b}$, in keeping with the penetration model for the cap and film region. This is because for the range of parameter values listed in Table 1, the values of $Fo < 0.1$ and therefore the penetration model applies to the film.

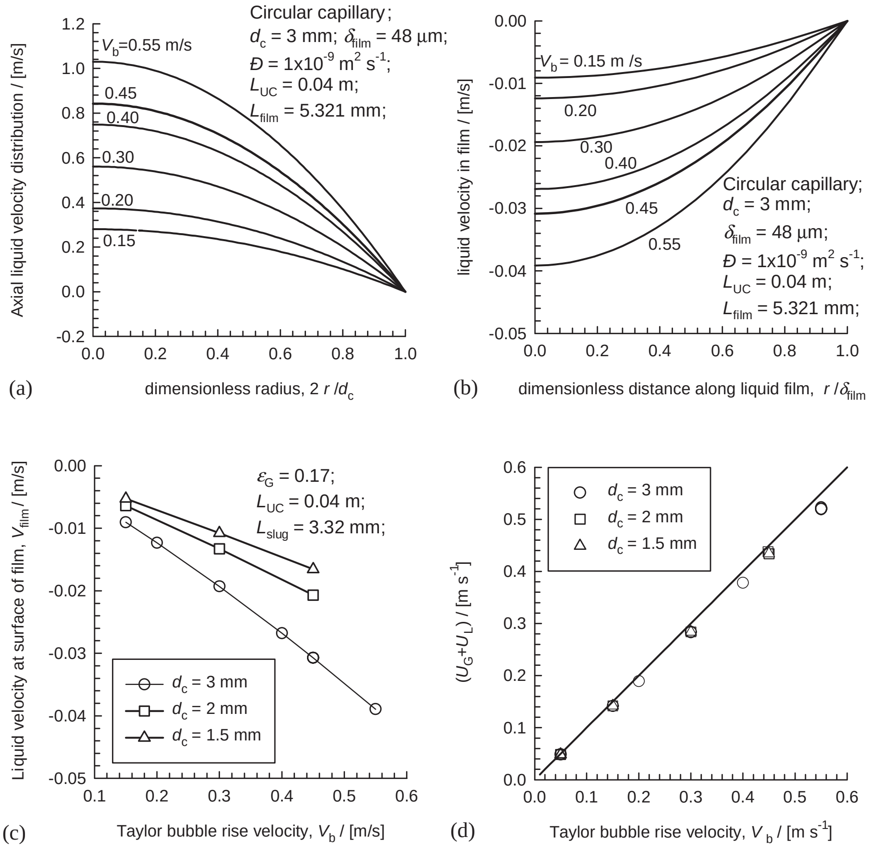

Fig. 4. Radial distribution of liquid velocity (a) at the outlet of the computational domain cell, and (b) within the film surrounding the bubble. In these simulation campaigns $d_c = 3$ mm, $V_b = 0.45$ m/s, $L_{UC} = 0.04$ m, $\delta_{\mathrm{film}} = 48$ µm, $\varepsilon_G = 0.17$, $L_{\mathrm{film}} = 5.321$ mm, $Ð = 1 \times 10^{-9}$ m^2/s. The velocity profiles in (a) and (b) are in the reference frame with respect to a stationary wall. (c) Dependence of surface velocity of the liquid film on the bubble rise velocity V_b for different channel diameters, $d_c = 1.5$ mm ($\delta_{\mathrm{film}} = 24$ µm, $L_{\mathrm{film}} = 6.289$ mm), 2 mm ($\delta_{\mathrm{film}} = 32$ µm, $L_{\mathrm{film}} = 5.966$ mm) and 3 mm ($\delta_{\mathrm{film}} = 48$ µm, $L_{\mathrm{film}} = 5.321$ mm). (d) Dependence of $(U_G + U_L)$ on the bubble rise velocity V_b for channel diameters $d_c = 1.5$ mm($\delta_{\mathrm{film}} = 24$ µm, $L_{\mathrm{film}} = 6.289$ mm), 2 mm ($\delta_{\mathrm{film}} = 32$ µm, $L_{\mathrm{film}} = 5.966$ mm) and 3 mm ($\delta_{\mathrm{film}} = 48$ µm, $L_{\mathrm{film}} = 5.321$ mm).

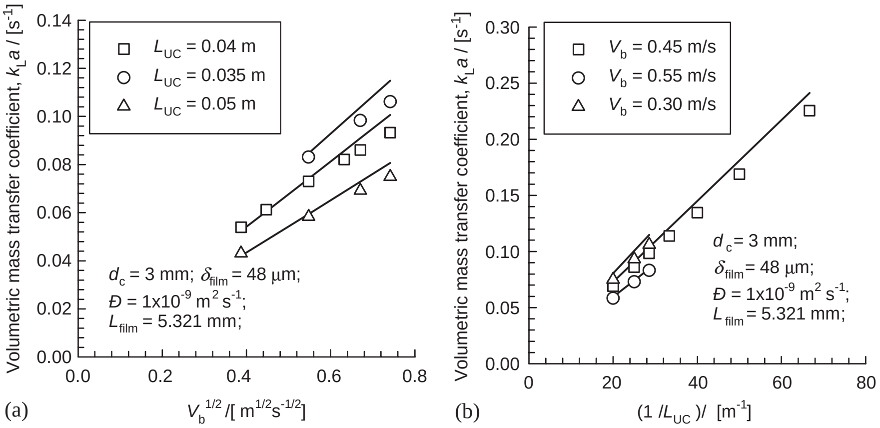

Fig. 5. Dependence of the volumetric mass transfer coefficient on (a) bubble rise velocity, and (b) unit cell length. In these simulation campaign $d_c = 3$ mm, $\delta_{\text{film}} = 48$ μm, $\varepsilon_G = 0.17$, $L_{\text{film}} = 5.321$ mm, and $Đ = 1 \times 10^{-9}$ m^2/s. The continuous lines represent calculations using Eqs. (2), (3), (9),(10) and (24).

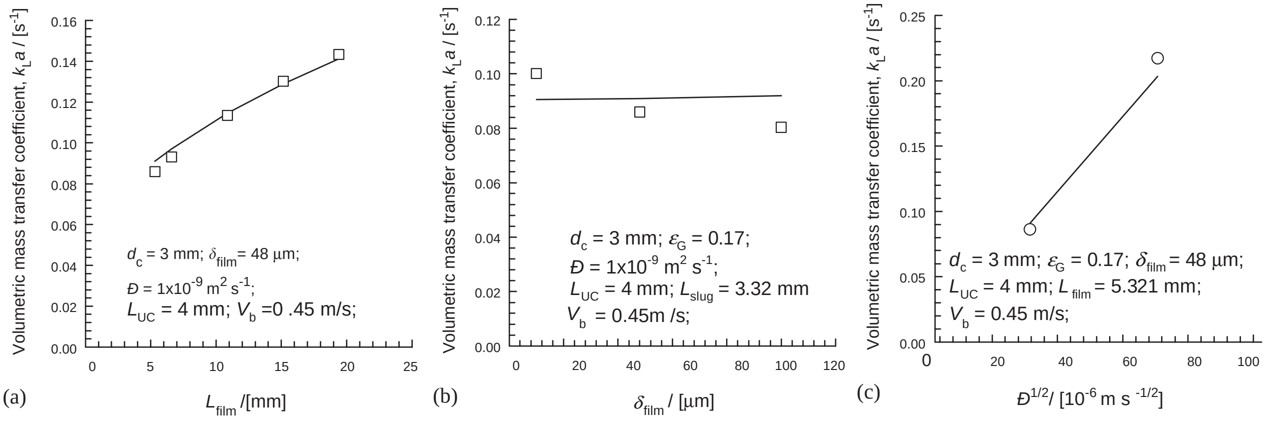

Fig. 6. Dependence of the volumetric mass transfer coefficient on (a) length of liquid film, (b) thickness of liquid film, and (c) liquid phase diffusivity. In these simulation campaigns $d_c = 3$ mm, $V_b = 0.45$ m/s, $L_{UC} = 0.04$ m. The continuous lines represent calculations using Eqs. (2), (3), (9),(10) and (24).

For the bulk of the simulations performed in this the contribution of the film amounted to 60–80% of the overall $k_L a$ values. The continuous lines in Fig. 5a represent the calculations using

$$k_L a = k_{L,\text{cap}} a_{\text{cap}} + k_{L,\text{film}} a_{\text{film}} \tag{24}$$

using Eqs. (2), (3), (9) and (10). The agreement between the CFD simulated $k_L a$ values with Eq. (24) is very good, for a range of unit cell lengths $L_{UC} = 0.035, 0.04$ and 0.05 m.

From Eq. (24) we should also expect $k_L a$ to show an inverse dependence on the unit cell length, L_{UC}. This is indeed found to be the case for simulation campaigns in which the unit cell length is varied for a constant bubble rise velocity; see Fig. 5b.

When the length of the liquid film L_{film} is increased, there are two opposing outcomes. The interfacial area a_{film} increases, while the $k_{L,\text{film}}$ decreases. The overall result is a less-than-proportionate increase in the $k_L a$; this is seen in Fig. 6a.

Fig. 6b shows the influence of varying film thickness $\delta_{\text{film}} = 10, 48$ and 100 μm on $k_L a$. Our simple model Eq. (24) predicts that the $k_L a$ is independent of the film thickness, because both cap and film mass transfers take place in the penetration regime. The CFD simulations show a minor dependence of $k_L a$ on δ_{film}, perhaps due to grid convergence differences for thin and thick films. The simulation results presented in Fig. 6c for the influence of the liquid phase diffusivity $Đ$, confirms the square-root dependence suggested by the penetration model for *both* cap and film regions.

In sharp contrast to the findings of the Bercic–Pintar correlation (1), Eq. (24) anticipates a dependence of $k_L a$ on the channel diameter d_c. This is because $k_{L,\text{cap}}$ is inverse proportional to $\sqrt{d_c}$ and a_{film} is inverse proportional to d_c. The simulation results for 1.5, 2 and 3 mm channels, for (a) varying bubble rise velocity and (b) varying unit cell length, confirm this channel diameter dependence; see Fig. 7a,b. We also note that Eq. (24) captures the d_c influence correctly. For the 1.5 mm diameter capillary the predictions of $k_L a$ using

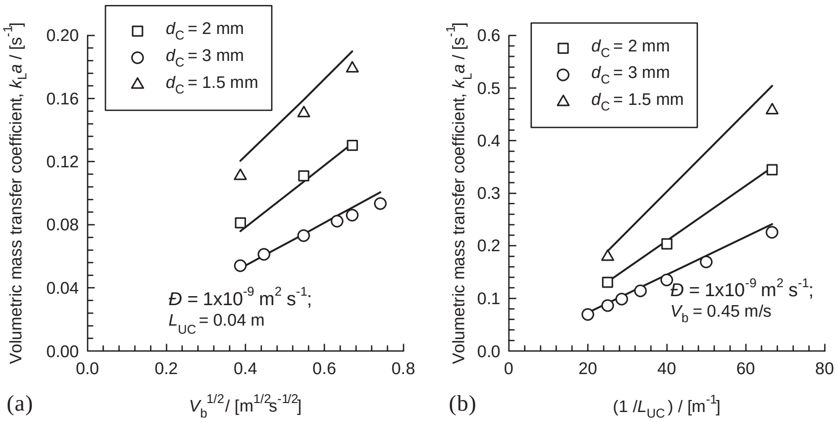

Fig. 7. Dependence of the volumetric mass transfer coefficient on (a) $\sqrt{V_b}$ and (b) $1/L_{UC}$ for the channel diameters $d_c = 1.5$ mm ($\delta_{\mathrm{film}} = 24$ μm, $L_{\mathrm{film}} = 6.289$ mm), 2 mm ($\delta_{\mathrm{film}} = 32$ μm, $L_{\mathrm{film}} = 5.966$ mm) and 3 mm ($\delta_{\mathrm{film}} = 48$ μm, $L_{\mathrm{film}} = 5.321$ mm). The continuous lines represent calculations using Eqs. (2), (3), (9),(10) and (24).

Eq. (24) are slightly higher than the CFD simulated values perhaps due to overestimation of the contribution of the film mass transfer.

It is interesting to compare our CFD simulation results with the Bercic–Pintar correlation (1). Since the diffusivity values used in our simulations, $Đ = 1 \times 10^{-9}$ m^2/s, are lower than the value in their experiments (diffusivity of methane in water, $Đ = 2 \times 10^{-9}$ m^2/s, interpolated using the experimental data reported by Poling et al. (2001)), the CFD simulated $k_L a$ need to be multiplied by $\sqrt{2}$, when comparing with Eq. (1). Fig. 8a presents a comparison of Eq. (1) with the experimental $k_L a$ data of Bercic and Pintar (1997) and the CFD simulated $k_L a$ values for 1.5 mm diameter channel. The agreement between the experiment and CFD simulations is remarkably good. It must however be remarked that data of Bercic and Pintar were obtained with relatively large unit cells, up to 0.22 m in length, leading to values of $k_L a$ largely in the 0.01–0.3 s^{-1} range. Our CFD simulations cover the practically more important range of values for $L_{UC} = 0.015$–0.05 m, yielding significantly higher $k_L a$ in the 0.1–0.7 s^{-1} range. Fig. 8b presents a comparison of Eq. (1) with the experimental $k_L a$ data of Bercic and Pintar (1997) obtained with a 2.5 mm capillary with the CFD simulated $k_L a$ values for 2 mm diameter channel. There is reasonable agreement with CFD simulated values and experiment but we note that the CFD simulations tend to yield lower $k_L a$ values than predicted by Eq. (1), with increasing values of $(U_G + U_L)^{1.19}/((1 - \varepsilon_G)L_{UC})^{0.57}$. The comparison of the $k_L a$ data of Bercic for 3.1 mm channel are compared with CFD simulations in Fig. 8c. There is only a small region of overlap of the data. The CFD simulations yield significantly lower $k_L a$ values than predicted by Eq. (1).

In order to reconcile the Bercic–Pintar experimental data with the mass transfer model developed in this paper we examined their data carefully and eliminated those for which the estimated contact time for the film t_{film} was such as to yield high Fo and therefore close-to-saturation conditions. From the remainder of the data we selected a set where the unit cell length was kept constant in the range $L_{UC} = 0.057$–0.058 m. The experimental $k_L a$ values for this selected data set are plotted in Fig. 8d against $\sqrt{V_b}$. We note that $k_L a$ values show a linear dependence on $\sqrt{V_b}$ in keeping with the penetration model for both cap and film regions. Furthermore we see that the data for 1.5 mm diameter capillary are systematically higher than those for the 2.5 and 3.1 mm diameter capillaries. This observation is entirely in line with our CFD simulations shown in Fig. 7a.

We must conclude that for large values of bubble rise velocity, and small unit cells, the predictions of Eq. (1) are not good and do not reflect the influence of the channel diameter on $k_L a$.

5. Conclusions

CFD simulations have been used to validate a fundamental model for mass transfer from Taylor bubbles to the surrounding liquid, given by Eqs. (2), (3), (9), (10) and (24), involving the sum of the contributions of the "cap" and "film" regions. This model shows that $k_L a$ is affected by several parameters including the bubble rise velocity V_b, unit cell length L_{UC}, length of liquid film L_{film}, liquid diffusivity $Đ$, and the channel diameter d_c. The CFD simulations of $k_L a$ for 1.5 mm capillary agree remarkably well with the experimental data of Bercic and Pintar (1997), and also the predictions of their empirical correlation given by Eq. (1). However, for larger channel diameters the CFD simulations show a significant deviation from the predictions of Eq. (1)

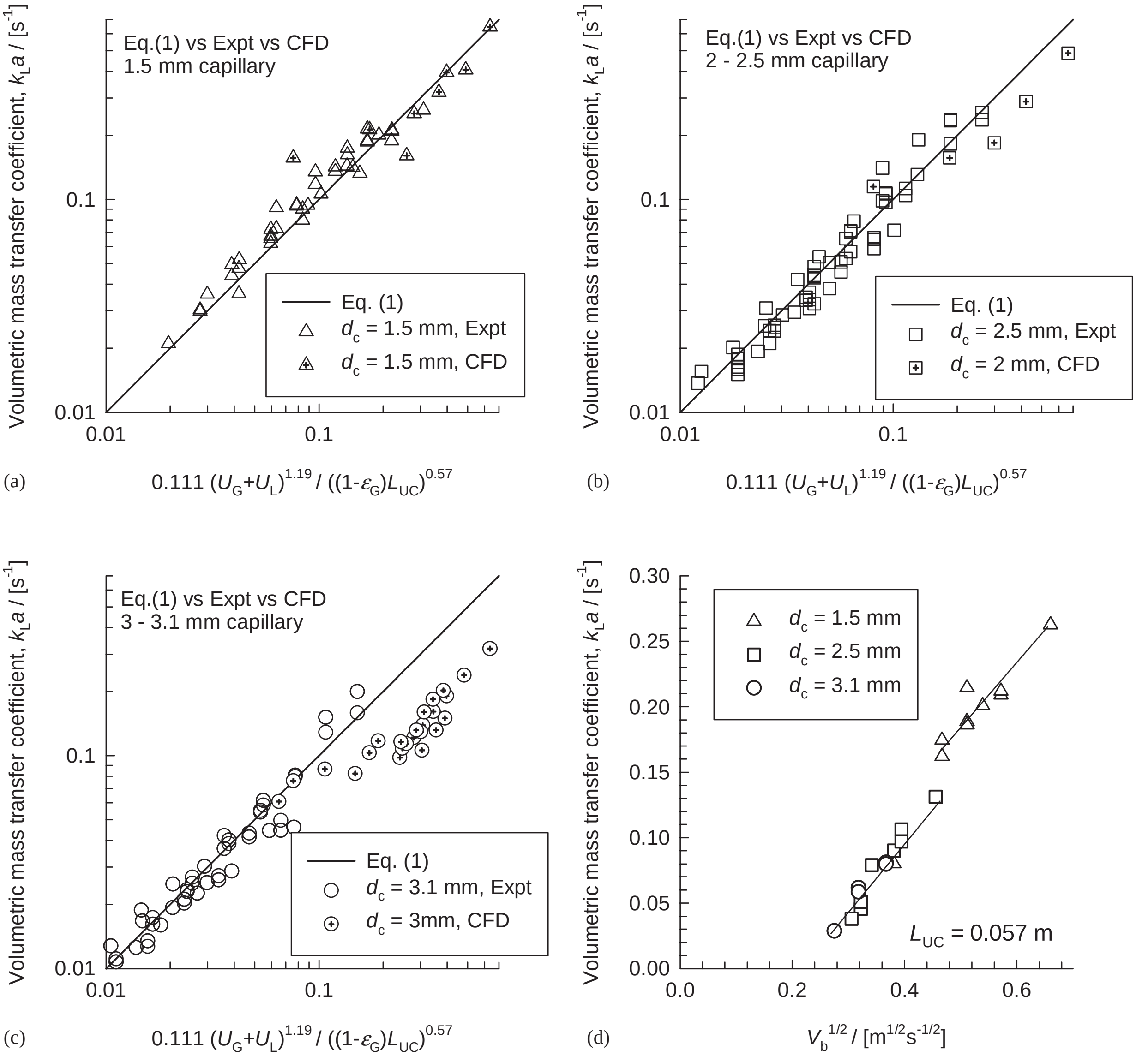

Fig. 8. Comparison of Eq. (1) with experimental data of Bercic and Pintar (1997) and CFD simulated k_La values for (a) 1.5 mm, (b) 2–2.5 mm and (c) 3–3.1 mm capillaries. Note that the CFD simulated values are multiplied by $\sqrt{2}$ in order to "correct" for the liquid phase diffusivity. The U_G and U_L values were obtained from the CFD simulations using Eqs. (16) and(14), respectively, (d) Experimental data of Bercic and Pintar (1997) plotted against $\sqrt{V_b}$.

especially for large values of bubble rise velocity, and small unit cells.

The developed fundamental model provides good prediction of k_La over a wide range of parameter values and provides a more reliable procedure for estimation of gas–liquid mass transfer coefficients in monolith reactors.

Notation

a	gas–liquid interfacial area per unit cell volume, m^2/m^3
A	cross sectional area, m^2
C	concentration of tracer in liquid phase, a.u.
Ca	Capillary number, dimensionless
d_c	capillary diameter, m
d_b	bubble diameter, m
$Đ$	liquid phase diffusivity, m^2/s
Fo	Fourier number for diffusion in liquid film, dimensionless
$\mathbf{g}$	gravitational vector, m s^{-2}
k_L	liquid phase mass transfer coefficient, m/s
L_{slug}	length of liquid slug; see Fig. 1(a), m
L_{UC}	unit cell length, m
L_{film}	length of liquid film; see Fig. 1(a), m
n	vector normal to the surface, dimensionless
p	system pressure, Pa
Q_{film}	volumetric liquid film flow; m^3/s

r	radial coordinate, m
t	time, s
t_{film}	contact time of liquid film with Taylor gas bubble, m/s
$\mathbf{u}$	liquid velocity vector, m/s
u	velocity in z-direction, m/s
U_G	superficial gas velocity, m/s
U_L	superficial liquid velocity, m/s
U_{LS}	mean velocity of liquid slug, m/s
V_b	Taylor bubble rise velocity, m/s
V_{film}	velocity at surface of liquid film, next to bubble, m/s
V_{wall}	velocity of wall boundary condition in simulations, equal to V_b, m/s
z	axial coordinate, m

Greek letters

δ_{film}	thickness of film surrounding bubble, m
Δ	parameter defined by Eq. (7), dimensionless
ε_G	gas holdup, dimensionless
μ_L	liquid viscosity, Pa s
ρ_L	density of liquid phase, kg/m^3
σ	surface tension, N/m^1

Subscripts

b	refers to Taylor bubble
bottom	bottom boundary of computational domain
c	refers to capillary
cap	refers to hemispherical cap
domain	in computational space
film	refers to liquid film
G	refers to gas phase
i	referring to cell number i
L	refers to liquid phase
s	at the bubble surface
top	top boundary of computational domain
UC	refers to unit cell
wall	refers to wall
z	in axial direction
$\perp$	perpendicular

Acknowledgements

We are grateful to Dr. G. Bercic for providing us the experimental data reported in his 1997 paper in electronic format for re-plotting purposes. We are also extremely grateful to Dr. Bercic for his critical comments on the manuscript. The Netherlands Organisation for Scientific Research (NWO) is gratefully acknowledged for providing financial assistance in the form of a "programmasubsidie" for development of novel concepts in reactive separations technology.

References

Aussillous, P., Quere, D., 2000. Quick deposition of a fluid on the wall of a tube. Physics of Fluids 12, 2367–2371.

Bercic, G., Pintar, A., 1997. The role of gas bubbles and liquid slug lengths on mass transport in the Taylor flow through capillaries. Chemical Engineering Science 52, 3709–3719.

Boger, T., Roy, S., Heibel, A.K., Borchers, O., 2003. A monolith loop reactor as an attractive alternative to slurry reactors. Catalysis Today 79, 441–451.

Crynes, L.L., Cerro, R.L., Abraham, M.A., 1995. Monolith froth reactor—development of a novel 3-phase catalytic-system. American Institute of Chemical Engineers Journal 41, 337–345.

de Deugd, R.M., Chougule, R.B., Kreutzer, M.T., Meeuse, F.M., Grievink, J., Kapteijn, F., Moulijn, J.A., 2003a. Is a monolithic loop reactor a viable option for Fischer–Tropsch synthesis? Chemical Engineering Science 58, 583–591.

de Deugd, R.M., Kapteijn, F., Moulijn, J.A., 2003b. Using monolithic catalysts for highly selective Fischer–Tropsch synthesis. Catalysis Today 79, 495–501.

Edvinsson, R.K., Cybulski, A., 1995. A comparison between the monolithic reactor and the trickle-bed reactor for liquid-phase hydrogenations. Catalysis Today 24, 173–179.

Edvinsson, R.K., Holmgren, A.M., Irandoust, S., 1995. Liquid-phase hydrogenation of acetylene in a monolithic catalyst reactor. Industrial & Engineering Chemistry Research 54, 94–100.

Heiszwolf, J.J., Kreutzer, M.T., van den Eijnden, M.G., Kapteijn, F., Moulijn, J.A., 2001. Gas–liquid mass transfer of aqueous Taylor flow in monoliths. Catalysis Today 69, 51–55.

Irandoust, S., Andersson, B., 1988a. Monolithic catalysts for non-automobile applications. Catalysis Reviews-Science and Engineering 30, 341–392.

Irandoust, S., Andersson, B., 1988b. Mass-transfer and liquid-phase reactions in a segmented 2-phase flow monolithic catalyst reactor. Chemical Engineering Science 43, 1983–1988.

Irandoust, S., Andersson, B., 1989. Simulation of flow and mass-transfer in Taylor flow through a capillary. Computers & Chemical Engineering 13, 519–526.

Irandoust, S., Gahne, O., 1990. Competitive hydrodesulfurization and hydrogenation in a monolithic reactor. American Institute of Chemical Engineers Journal 36, 746–752.

Irandoust, S., Ertle, S., Andersson, B., 1992. Gas–liquid mass-transfer in Taylor flow through a capillary. Canadian Journal of Chemical Engineering 70, 115–119.

Kapteijn, F., Nijhuis, T.A., Heiszwolf, J.J., Moulijn, J.A., 2001. New non-traditional multiphase catalytic reactors based on monolithic structures. Catalysis Today 66, 133–144.

Klinghoffer, A.A., Cerro, R.L., Abraham, M.A., 1998. Influence of flow properties on the performance of the monolith froth reactor for catalytic wet oxidation of acetic acid. Industrial & Engineering Chemistry Research 37, 1203–1210.

Kreutzer, M.T., 2003. Hydrodynamics of Taylor flow in capillaries and monolith reactors. Ph.D. Thesis, Delft University of Technology, Delft, The Netherlands.

Kreutzer, M.T., Du, P., Heiszwolf, J.J., Kapteijn, F., Moulijn, J.A., 2001. Mass transfer characteristics of three-phase monolith reactors. Chemical Engineering Science 56, 6015–6023.

Nijhuis, T.A., Kreutzer, M.T., Romijn, A.C.J., Kapteijn, F., Moulijn, J.A., 2001. Monolithic catalysts as more efficient three-phase reactors. Catalysis Today 66, 157–165.

Nijhuis, T.A., Dautzenberg, F.M., Moulijn, J.A., 2003. Modeling of monolithic and trickle-bed reactors for the hydrogenation of styrene. Chemical Engineering Science 55, 1113–1124.

Poling, B.E., Prausnitz, J.M., O'Connell, J.P., 2001. The Properties of Gases and Liquids, 5th Edition. McGraw-Hill, New York.

Rhie, C.M., Chow, W.L., 1983. Numerical study of the turbulent flow past an airfoil with trailing edge separation. A.I.A.A. Journal 21, 1525–1532.

Sherwood, T.K., Pigford, R.L., Wilke, C.R., 1975. Mass Transfer. Mc-Graw Hill, New York, USA.

Stankiewicz, A., 2001. Process intensification in in-line monolithic reactor. Chemical Engineering Science 56, 359–364.

Thulasidas, T.C., Abraham, M.A., Cerro, R.L., 1995. Bubble-train flow in capillaries of circular and square cross-section. Chemical Engineering Science 50, 183–199.

van Baten, J.M., Krishna, R., 2004. Mass Transfer for Taylor flow in Capillaries, University of Amsterdam, Amsterdam, The Netherlands, 12 March 2004, http://ct-cr4.chem.uva.nl/taylor_cfd.

van Doormal, J., Raithby, G.D., 1984. Enhancement of the SIMPLE method for predicting incompressible flows. Numerical Heat Transfer 7, 147–163.

Vandu, C.O., Ellenberger, J., Krishna, R., 2004. Taylor bubble rise in circular and square capillaries. University of Amsterdam, Amsterdam, The Netherlands, 16 January 2004, http://ct-cr4.chem.uva.nl/SingleCapillary/.